Icarus 420 (2024) 116212

Contents lists available at ScienceDirect

Icarus

journal homepage: www.elsevier.com/locate/icarus

Kinetic simulations of dust grain charging in experimental plasma conditions

David Lund [a], Nikolaos A. Gatsonis [b], Daoru Han [a,*]

[a] Department of Mechanical and Aerospace Engineering, Missouri University of Science and Technology, 400 W. 13th St., Rolla, 65409, MO, USA
[b] Department of Aerospace Engineering, Worcester Polytechnic Institute, Worcester, 01609, MA, USA

ARTICLE INFO

Keywords:
Dusty plasma
Dust charging
Kinetic simulations

ABSTRACT

This paper presents fully-kinetic numerical investigations of the charging of spherical and irregular dust grains in the OML sheath regime and a stationary experimental plasma environment utilizing the Dusty Parallel Immersed-Finite-Element Particle-in-Cell (PIFE-PIC-D) framework. The simulations account for surface charging of the dust grains immersed in an stationary plasma environment. PIFE-PIC-D explicitly resolves the geometrical and material properties (permittivity) of each individual dust grain. The charge collection over time of each dust grain is investigated with varying size, irregularity, number of grains, spacing between dust grains, and permittivity. The charging behavior of a dust cluster is estimated by calculating its electron Debye length edge-to-edge separation to offer valuable insights into a dust cluster's general charge dynamics. Lastly, unlike prior studies that focused solely on either fully conducting spheres or perfectly dielectric spheres, this work explores a more comprehensive range of permittivities for irregular dust grain aggregates.

1. Introduction

Solid grains (particulates) which are much larger than the ions within a plasma are referred to as dusty plasmas and are present in many space environments. Several investigations, experiments, and simulations have been conducted to study the plasma–dust interactions in various environments Melzer et al. (1994), Cui and Goree (1994), Robertson et al. (1995), Northrop and Birmingham (1996), Matsoukas and Russell (1997), Vaulina et al. (1999), Bouchoule (1999), Smith et al. (2001), Flanagan and Goree (2006), Abbas et al. (2007), Khrapak et al. (2007), Gopalakrishnan and Hogan (2012), Sharma et al. (2012), Matthews et al. (2013), Ding et al. (2013), Anuar et al. (2013), Shotorban (2014), Hess et al. (2015), Picard and Girshick (2016), Asnaz et al. (2018), Chahl and Gopalakrishnan (2019), Vijayan et al. (2020), Matthews et al. (2020) and Zhao et al. (2021). Initial studies have looked into microscopic dust charging (on the grain-to-grain scale) as well as macroscopic dust transport scales (e.g. dust mobility within a lunar crater). Even early modeling approaches (in the 1990s) for dusty plasmas around spacecrafts utilized particle-in-cell Monte Carlo collision (PIC-MCC) with a multi-step Monte Carlo algorithm to track the plasma species' and dust grains' collisional absorption and solve the electric fields through Poisson's equation (Conger and Hastings, 1992; Gatsonis et al., 1994). Also early on, Erlandson and Gatsonis (1994) found that dust clouds of low density do not perturb the plasma's electric potential. In addition, dust clouds of high density create a sheath formation from the potential, and a double layer outside the cloud boundary is formed from the charge. This uncovered that the dust can be controlled by controlling the spacecraft potential.

In 2010, Matyash et al. (2010) investigated the charging of micrometer sized grains in low temperature plasmas. The grain (microscopic) scale utilized the particle–particle, particle-mesh (P3M) approach to track the plasma particles' trajectories very close to the dust grain, which allowed the dust grain charging from plasma particle absorption as well as ion drag forces from the transfer of momentum between drifting ions/dust grains to be modeled. This approached resulted in a full-scale kinetic representation of the background plasma and dust grain charging.

In 2016, Wang et al. (2016) introduced a grain-scale charging model, the "patched charge model", taking the capacitance of an isolated spherical dust grain plus the experimentally defined empirical constants to predict Q_d/e (the amount of charge on a single dust grain) on the order of approximately 10^4. The model takes into account the micro-cavities between neighboring grains of dust which emit and reabsorb photoelectrons/secondary electrons. The newly accounted for micro-cavities generate large negative charges allowing the particle–particle repulsive forces to loft surface dust grains.

Also in 2016 and under a comparable plasma environment to the patched charge model, Zimmerman et al. (2016) showcased a test-particle approach (supercharging model) which used a multipole electric field solver and a boundary-element-based surface charging method that predicted Q_d/e on the order of approximately 10^2. The key points

* Corresponding author.
E-mail address: handao@mst.edu (D. Han).

https://doi.org/10.1016/j.icarus.2024.116212
Received 16 October 2023; Received in revised form 27 June 2024; Accepted 2 July 2024
Available online 9 July 2024

in their study concluded supercharged dust grains on the Moon can frequently go through dielectric breakdown, and electric fields between grains can become orders of magnitude larger than in traditionally predicted sheaths.

In 2019, Oudayer et al. (2019) investigated charging of a multi-layer pile of dust grains under vacuum ultra-violet (VUV) illumination through the Spacecraft Plasma Interactive Software (SPIS). On the first two layers, the grains acquired both negatively and positively charged patches, but the deeper layers tended to charge more negative due to only the collection of electrons. Their simulations reinforced the grain supercharging model from other studies. Although, they also showed the charging may be limited by the dust electrical properties. Despite these previous studies, a fundamental question about dusty plasma remains open: what is the net amount of charge and distribution/fluctuation (thus electrodynamic forces) on each individual dust grain in a dusty plasma?

This study focuses on the electrostatic interactions in dusty plasmas, particularly, charging of dust particulates in the collisionless regimes. A most recently developed fully-kinetic particle simulation code, namely, Dusty Parallel Immersed-Finite-Element Particle-in-Cell (PIFE-PIC-D), will be utilized to self-consistently resolve the plasma environment and charging of immersed materials. This model explicitly includes the materials property (dielectric constant) of the dust grains. The remaining paper is organized as follows: Section 2 briefly describes the PIFE-PIC-D code. Section 3 provides several code validation cases of dust grain charging in the OML sheath regime as well as in a stationary experimental plasma environment. Section 4 discusses the novel simulation results of spherical and irregular dust charging in a stationary experimental plasma with varying irregularity, spacing between dust grains, and permittivity. Lastly, Section 5 contains a summary and conclusion.

2. The PIFE-PIC-D code

In PIFE-PIC-D, the computation domain is first decomposed into cubic blocks with the same PIC mesh size. Local (not necessarily uniform) IFE mesh is then generated for each sub-domain. The data interaction between IFE and PIC meshes within each sub-domain is described in detail in Ref. Kafafy and Wang (2006).

For the parallel electrostatic field solver, Dirichlet-Dirichlet domain decomposition with overlapping cells is used to distribute the sub-domains among multiple MPI processes (Smith et al., 1996). For each sub-domain, the IFE solver is the same as the sequential IFE method with Dirichlet boundary conditions (He et al., 2008, 2011). These Dirichlet boundary conditions are imposed at the boundaries of the sub-domains, which are also interior for the neighboring sub-domains. Therefore, the field solution at respective neighboring sub-domains are used as Dirichlet boundary conditions for each sub-domain. Within each field-solve step, inner iterations are performed such that the solutions of the overlapping cells are exchanged and updated as the new Dirichlet boundary conditions for the respective neighboring sub-domains.

In the PIFE-PIC-D framework, simulation particles belonging to a certain sub-domain are stored together on the processor that solves the field of the same sub-domain. In this sense, "particle quantities" and "field quantities" of each sub-domain are handled by the same processor. Data communications are implemented at inner boundaries for needed calculations such as charge-weighting of the PIC method. More details of PIFE-PIC and its verification/validation studies are given in Ref. Han et al. (2018, 2021) and Lund et al. (2022).

All plasma particles in this paper follow the Maxwellian distributions. For a drifting Maxwellian population, the normalized velocity distribution function, $\hat{f}_m(v)$, is defined as:

$$\hat{f}_m(v) = \frac{1}{v_{th}\sqrt{\pi}} exp[-\frac{(v - v_d)^2}{(v_{th})^2}], \tag{1}$$

where v_{th} is the thermal velocity and v_d is the drifting velocity. The velocity sampling for the pre-loaded particles is using a full Maxwellian distribution, but only a part of the velocity distribution range is required for particle injection at the global boundaries since only those going into the domain are sampled. The drifting Maxwellian form is defined because the code suite can account for drifting plasmas, but due to the cases in this paper being a stationary plasma, v_d is set to 0.

Due to differing media on both sides of the interface, Γ, the electric field, E, is discontinuous across the object's surface. Therefore, the electrostatic field on both sides of the boundary interface, Γ, must be considered to obtain the electric field flux condition:

$$\left[\varepsilon \frac{\partial \phi}{\partial \mathbf{n}}\right]\Big|_{\Gamma} = -\left(\varepsilon_2 \mathbf{E}_2 - \varepsilon_1 \mathbf{E}_1\right) \cdot \mathbf{n} = -\sigma_s, \tag{2}$$

where $\mathbf{n}$ is the normal vector from Medium 1 to Medium 2, ε is the permittivity of the object, and σ_s is the surface charge density. The square brackets indicate the jump condition of the function. The subscripts 1&2 denote Medium 1 and Medium 2. By changing the permittivity of the object it affects the outcome of the electric fields, surface potential, and surface charge. More details for the description and formulation of the flux jump condition across the interface are given in Han et al. (2016b).

In PIC methods, it is a common practice to use a dimensionless unit system; therefore, normalized units are used within the PIFE-PIC-D code package to diminish round-off errors due to some numerical values being too large or small within the simulation. The reference parameters used for normalization are selected as electron parameters since they are much more mobile than ions within the PIC simulations. For example, the electron density, temperature, frequency, and Debye length are used as the normalization references in this paper.

3. Code validation

This section provides several code validation cases of dust grain charging in the OML sheath regime as well as in a stationary experimental plasma environment.

3.1. Code validation in the OML sheath regime

The PIFE-PIC-D code suite is applied to simulate a small dielectric sphere charging in a collisionless and stationary plasma environment known as the orbital-motion-limited (OML) sheath regime. Previously, successful validations of the IFE-PIC and PIFE-PIC code suites were compared against the analytic OML solutions (Han et al., 2016b,a, 2021). This section extends these successful validations by conducting a comparison study on varying the permittivity of the dust grain.

3.1.1. Problem description and simulation setup

A stationary, collisionless hydrogen plasma with equal ion and electron temperatures ($T_i = T_e$) is considered. The revised OML theory (Tang and Delzanno, 2014; Delzanno and Tang, 2015) gives the ion and electron densities' analytic expressions. To get the analytic potential profile around the sphere, Poisson's equation can be numerically solved in spherical coordinates. The PIC method uses simulation particles (known as macro-particles or super-particles) to represent the real plasma particles. The simulations within Section 3.1 average 6,400,000 simulation particles at the simulation's steady-state, which includes 3,000,000 simulation electrons and 3,400,000 simulation ions.

3.1.2. Computation domain and mesh

A computation domain of a $3 \times 3 \times 3$ Debye cube with a uniform PIC mesh of $h = 0.1\lambda_D$ is used in all three directions, where h is the cell width and λ_D is the Debye length of the plasma. The computation domain has $30 \times 30 \times 30 = 27{,}000$ PIC cells ($27{,}000 \times 5 = 135{,}000$ tetrahedral FE/IFE cells as each is partitioned into 5 tetrahedral FE/IFE cells) (Han et al., 2016b,a). The IFE mesh size is also globally uniform

within the simulations. The dust grain modeled as a sphere is treated as either a dielectric or a conductor and is centered at the origin with a normalized radius of $R_s = 0.501$ or approximately 2.0×10^{-5} m in physical units. Only 1/8 of the sphere is simulated in the domain due to symmetry of the setup. The domain is broken down to $3 \times 3 \times 3$ subdomains where one MPI process computes each subdomain.

3.1.3. Field setup

The reference potentials are set to 0 at the $X_{\max}$, $Y_{\max}$, and $Z_{\max}$ boundaries. Zero-Neumann boundary conditions are applied at the $X_{\min}$, $Y_{\min}$, and $Z_{\min}$ boundaries due to the symmetry of the domain. The sphere has a relative permittivity of 4, 40, 400, or 4000. The non-homogeneous flux jump condition from the surface of the sphere is used to calculate the sphere's floating potential. Here the non-homogeneous flux jump condition is the electric field jump across the object's interface due to surface charging and differing electrostatic fields on both sides of the interface (Han et al., 2016b).

The simulation is carried out using the realistic ion-to-electron mass ratio of $m_i/m_e = 1836$. Before the initial field solution, the simulation particles are pre-loaded into the domain. Also within each PIC step, the particles are injected at $X_{\max}$, $Y_{\max}$, and $Z_{\max}$. Particles are reflected due to symmetry when hitting the $X_{\min}$, $Y_{\min}$, and $Z_{\min}$ boundaries. Particles are absorbed and removed from the simulation when hitting the $X_{\max}$, $Y_{\max}$, and $Z_{\max}$ boundaries or when intersecting a dust grain's surface. There were 125 particles ($5 \times 5 \times 5$) per species, per cell that were loaded and/or injected into the domain.

3.1.4. Simulation results

All the simulations in this paper ran on the *Foundry* cluster provided by the Center of High-Performance Computing Research at Missouri University of Science and Technology. The computing nodes are configured with Dell C6525 nodes each having four node chassis with each node containing dual 32-core AMD EPYC Rome 7452 CPUs with 256 GB DDR4 RAM and six 480 GB SSD drives in RAID 0. These simulations ran for a total of 40,000 PIC steps, which well exceeds the PIC steps required for the simulation to reach quasi steady-state (shown later in the dust grain charging over time plots.) The time step size was set to be 0.05 resulting in a normalized time of $\hat{t} = 2000$, found by multiplying the number of PIC steps by the time step.

Fig. 1 compares the PIFE-PIC-D simulation results against analytic solution of the OML sheath. The potential profile agrees very well with the analytic solution for all varying permittivities. Also, it is expected that the varying permittivity of the spherical dust grains do not change the results, which is explained shortly. Details of the revised OML theory, including formulation, analytical solutions, and normalization factors can be found in Tang and Delzanno (2014).

In this paper, the net surface charge ratio of every dust grain is plotted with respect to the number of PIC steps. The net charge was determined by accumulating the number of deposited electrons and ions onto the surface of the partial or full dust grains. Then the number of ions was subtracted from the number of electrons (since the number of ions collected was less than the number of electrons due to the spheres charging negative.) The particles collected were simulation particles, so next the simulation particles were converted to physical particles by the normalization factor based on the plasma density divided by the number of particles in each cell in all three directions. Finally, the partial dust grain was multiplied by a symmetry factor to account for the particle collection of the full dust grain. For example, the particles collected by the 1/8 sphere at the origin were multiplied by 8.

For all the cases in this paper, the electron frequency is 9400 s^{-1} which is used to normalize the physical time. The electron plasma frequency is defined as:

$$w_{pe} = \sqrt{\frac{4\pi n_e e^2}{m_e}} \tag{3}$$

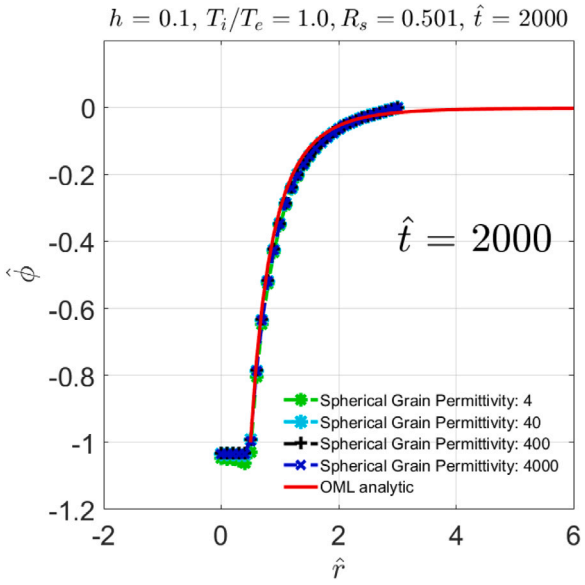

Fig. 1. 1-D potential profile of PIFE-PIC-D versus the OML analytical solution for varying permittivity of spherical dust grains with a permittivity of 4, 40, 400 and 4000. Where R_s is the normalized radius of the dust grain; $\hat{t}$, $\hat{\phi}$, and $\hat{r}$ are the normalized time, potential, and distance values, respectively. The flat region near $\hat{r} = 0$ is the normalized surface potential of the dust grain calculated from the non-homogeneous flux jump condition which results in the normalized potential values stored on the PIC mesh.

where the units are of s^{-1}, and m_e is the electron's mass, n_e is the electron number density, and e is the elementary charge. The simulations ran for $\hat{t} = 2000$, which is about a physical time of 0.213 s. This is a sufficient amount of time for multiple periods of the plasma frequency. It should be noted there are 0.05 PIC steps in one normalized time step.

Fig. 2 shows the net surface charge ratio, Q_d/e, over time for varying permittivity (4, 40, 400, and 4000) of spherical dust grains in the OML sheath regime, where Q_d is the surface charge of the dust grain and e is the elementary charge. The charge of the dust grain's surface will reach equilibrium when Q_d/e no longer fluctuates. For these cases, the charge stops fluctuating around 10,000 PIC steps resulting in quasi steady-state being reached.

From Fig. 2, the four different permittivities of the dust grains result in the same net surface charge on each dust grain. The dust grains all reached a net surface charge ratio, Q_d/e, of approximately 3.4×10^4. These four different permittivities resulted in the same net surface charge regardless of being treated as a dielectric or a conductor because the dust grain has spherical symmetry with no other dust grains surrounding it. This causes the impacts of the ions and electrons to uniformly distribute over the surface of the dust grain, which mirrors the property conductors have of rearranging themselves to be uniformly charged. Typically, dielectrics lack this ability to rearrange themselves and create equipotentials on their surface. Therefore, regardless of the grain's permittivity, a dielectric sphere with no other grains or surfaces close by will act as a spherical capacitor. These are expected results which have now been verified to further validate the PIFE-PIC-D code suite.

3.2. Charging of dust grains in a stationary experimental plasma environment

This section focuses on the charging of spherical dust grains in a stationary experimental plasma environment. The plasma environment parameters were retrieved from Ref. Flanagan and Goree (2006)'s experimental plasma conditions and are shown in Table 1. In the conducted study, three experimental conditions were tested; however,

Table 1
Experimental plasma conditions.

	Number density n, cm^{-3}	Drifting velocity v_d, $\times 10^7$ cm/s	Thermal velocity v_t, $\times 10^7$ cm/s	Temperature T, eV	Debye length λ_D, m
Electron	2.5×10^8	0	7.26	3	8.15×10^{-4}
Ion	2.5×10^8	0	0.017	0.03	8.15×10^{-5}

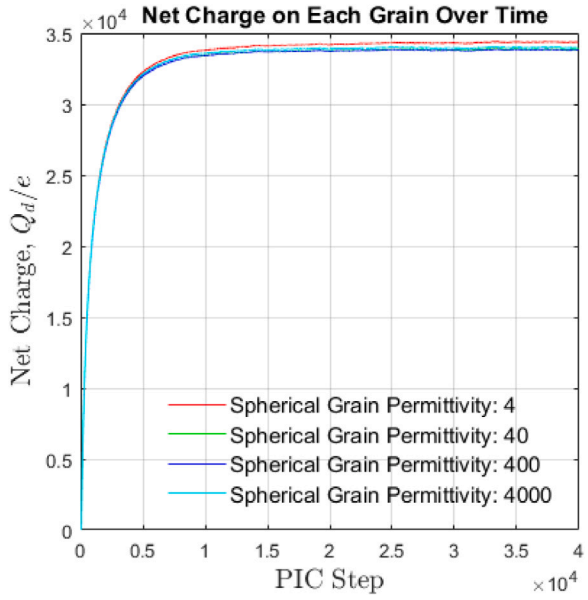

Fig. 2. Net surface charge for varying permittivity of spherical dust grains in the OML sheath regime including a spherical dust grain with a permittivity of 4, 40, 400, and 4000.

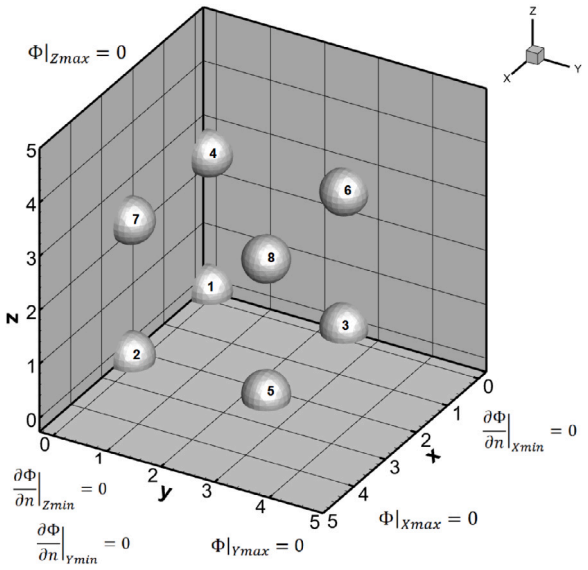

Fig. 3. 3-D IFE setup and boundary conditions shown for an eight partial grain configuration. The grains are numbered one through eight for identification later in the paper (the numbering is the same for the two and four partial dust grain cases).

our simulations will specifically target the condition featuring plasma without an electron beam. The plasma density and temperature in this experiment were measured using a Langmuir probe, ranging from 2.4×10^6 to 2.5×10^8 cm^{-3} and 3 to 16 eV (due to a bimodal electron distribution), respectively. The plasma thermal velocity and Debye length were then calculated using fundamental plasma physics equations. Numerous simulations were initially run within these specified plasma density and temperature ranges. In this work, we present results obtained with 2.5×10^8 cm^{-3} for the plasma density and 3 eV for the electron temperature as they provide the best conditions to confirm the validity of the PIFE-PIC-D code suite. The temperature of the ions is estimated as $T_i = 0.01T_e = 0.03$ eV due to the ions being close to room temperature and in thermal equilibrium with the neutral gas. This verification process will result in a robust code suite, instilling confidence in its applicability to challenging astrophysical environments where experimental data confirmation is limited.

The simulations within Section 3.2 average 25,000,000 to 30,000,000 simulation particles at the simulation's steady-state, where 40 to 50 percent are simulation electrons and 50 to 60 percent are simulation ions. The following simulations ran for a total of 40,000 PIC steps or $\hat{t} = 2000$. In Section 3.2, all the density values are normalized by 2.5×10^8 cm^{-3}, all the potential values are normalized by 3.0 V, and all the spatial dimensions are normalized by 8.15×10^{-4} m. These normalization parameters were selected as the electron density, temperature, and Debye length, respectively, from Table 1.

3.2.1. Computation domain and mesh

For these simulations, a $5 \times 5 \times 5$ Debye cube is the computation domain with a globally uniform PIC mesh of $h = 0.1\lambda_D$ in all three dimensions, where the Debye length of the plasma is λ_D. The simulation domain has $50 \times 50 \times 50 = 125{,}000$ PIC cells ($125{,}000 \times 5 = 625{,}000$ tetrahedral FE/IFE cells as each is partitioned into 5 tetrahedral FE/IFE cells) (Han et al., 2016b,a). The IFE mesh size is also globally uniform. Partial spheres are generated within the domain due to symmetry of the setup. The physical diameter of the dust grains is on the order of hundreds of micrometers. The size for the grain was chosen as a mid-sized grain due to its relevance in size compared to the lunar regolith. A mid-sized grain can more easily be handled when tested with experimentally for future comparison of results. The domain is broken down to $5 \times 5 \times 5$ subdomains where one MPI process computes each subdomain.

3.2.2. Field setup

The reference potentials are set to 0 at the $X_{\max}$, $Y_{\max}$, and $Z_{\max}$ boundaries. Zero-Neumann boundary conditions are applied at the $X_{\min}$, $Y_{\min}$, and $Z_{\min}$ boundaries due to the symmetry of the domain. The non-homogeneous flux jump condition from the surface of the sphere is used to calculate the sphere's floating potential. Fig. 3 illustrates the 3-D IFE setup and boundary conditions used in the simulations—here an eight partial grain configuration is shown with the individual grains numbered one through eight for future identification (the numbering is the same for the two and four partial dust grain cases.)

Before the initial field solution, the simulation particles are preloaded into the domain. Also within each PIC step, the particles are injected at $X_{\max}$, $Y_{\max}$, and $Z_{\max}$. Particles are reflected due to symmetry when hitting the $X_{\min}$, $Y_{\min}$, and $Z_{\min}$ boundaries. Particles are absorbed and removed from the simulation when hitting the $X_{\max}$, $Y_{\max}$, and $Z_{\max}$ boundaries or when intersecting a dust grain's surface. The normalized time step size was set to be 0.05. There are 125 particles ($5 \times 5 \times 5$) per species, per cell that were loaded and/or injected into the domain.

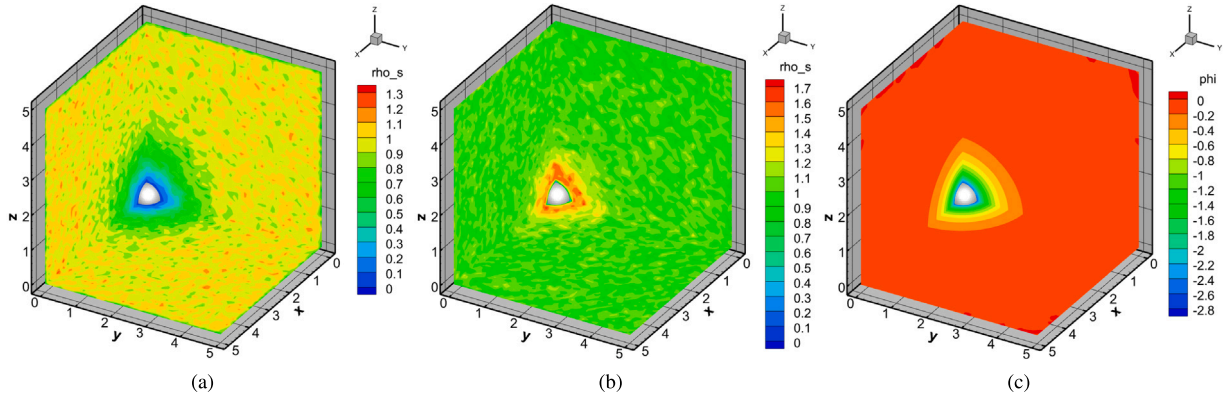

Fig. 4. Charging of a spherical dust grain with a normalized radius of 0.401 in a stationary experimental plasma including the (a) normalized electron density; (b) normalized ion density; and (c) normalized potential. (For interpretation of the references to colour in this figure legend, the reader is referred to the web version of this article.)

3.2.3. Simulation results

Varying Sized Single Dust Grains:

Here, three varying sized spherical dust grains with a normalized radius of $R_s = 0.201$, $R_s = 0.401$, or $R_s = 0.601$ are simulated. The dust grains are all dielectric with a permittivity of 4. Due to all three sizes adequately showing similar results, Fig. 4 was chosen to illustrate the normalized density contours of the ions and electrons as well as the normalized potential surrounding the varying sized spherical dust grains in a stationary experimental plasma for a dust grain with a normalized radius of $R_s = 0.401$. For the single sphere cases, only 1/8 of the sphere is generated within the domain due to the symmetry of the setup.

Fig. 5 shows the net surface charge ratio, Q_d/e, over time for varying sized spherical dust grains in a stationary experimental plasma. Where there are three different sized spheres which include a normalized radius of $R_s = 0.201$, $R_s = 0.401$, and $R_s = 0.601$. The charge stops fluctuating around 25,000 PIC steps for the $R_s = 0.201$ case and 15,000 PIC steps for the $R_s = 0.401$ and $R_s = 0.601$ cases, resulting in quasi steady-state being reached.

From Fig. 5, the three different sized dust grains result in a different net charge on each dust grain, although, on the same magnitude.

- For $R_s = 0.201$ (164 μm), Fig. 5a shows a net surface charge ratio, Q_d/e, of approximately 1.57×10^4.
- For $R_s = 0.401$ (327 μm), Fig. 5b shows a net surface charge ratio, Q_d/e, of approximately 2.74×10^4.
- For $R_s = 0.601$ (490 μm), Fig. 5c shows a net surface charge ratio, Q_d/e, of approximately 4.11×10^4.

These results show that the larger the dust grain, the more charge is accumulated. Since these dust grains are on the larger side, the charge on a single dust grain does not fluctuate with time resulting in an equilibrium for the current collected by the dust grain's surface. It is noted here that regardless of the dust grain's size, all the grains charge to the same normalized surface potential of approximately −2.8, as shown in the normalized potential subplot of Fig. 4c. Due to these isolated grains modeling a spherical capacitor, the maximum charge follows the relationship:

$$Q = C\phi, \tag{4}$$

where Q is the charge, C is the capacitance, and ϕ is the surface potential of the grain. The capacitance, C, is dependent on the square radius of the grain. Therefore, increasing the size of the grain will increase the charge on the grain, which is shown above. This relationship also shows that the surface potential, ϕ, of the grain is independent of its size, which is also consistent with the above results. These are expected

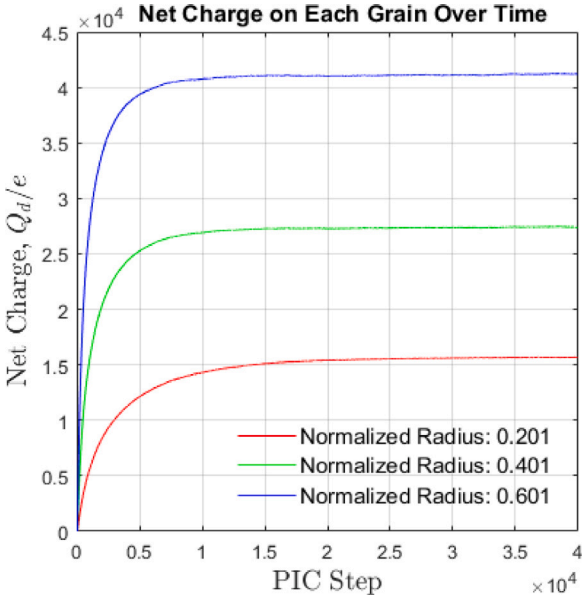

Fig. 5. Net surface charge for varying sized spherical dust grains in stationary experimental plasma including a spherical dust grain with a normalized radius of 0.201, 0.401, and 0.601.

results which have now been verified to further validate the PIFE-PIC-D code suite.

Multiple Dust Grain Configurations:

Figs. 6–8 illustrate the normalized density contours of the ions and electrons as well as the normalized potential surrounding the dust grains in multiple configurations in a stationary experimental plasma. For the multi-dust grain cases, 1/8 of the sphere is generated at the origin, 1/4 of the sphere is generated when the sphere is shifted only along one axis, 1/2 of the sphere is generated when the sphere is shifted along two axes, and the whole sphere is generated when the sphere is shifted along three axes (since the shift is larger than the sphere's radius) due to the symmetry of the setup. All the dust grains in this subsection have a normalized radius of $R_s = 0.401$ and are all dielectric with a permittivity of 4. In Fig. 6, there are two partial dust grains in the domain. In Fig. 7, there are four partial dust grains in the domain. In Fig. 8, there are eight partial dust grains in the domain. The dust grains are spaced $1.7\lambda_D$ edge-to-edge from neighboring grains. It is important to note that due to symmetry of the domain the two partial dust grain case is actually three full dust grains in a straight line, the four partial dust grain case is a cluster of seven full dust grains, and the eight partial dust grain case is a cluster of twenty-seven full dust grains.

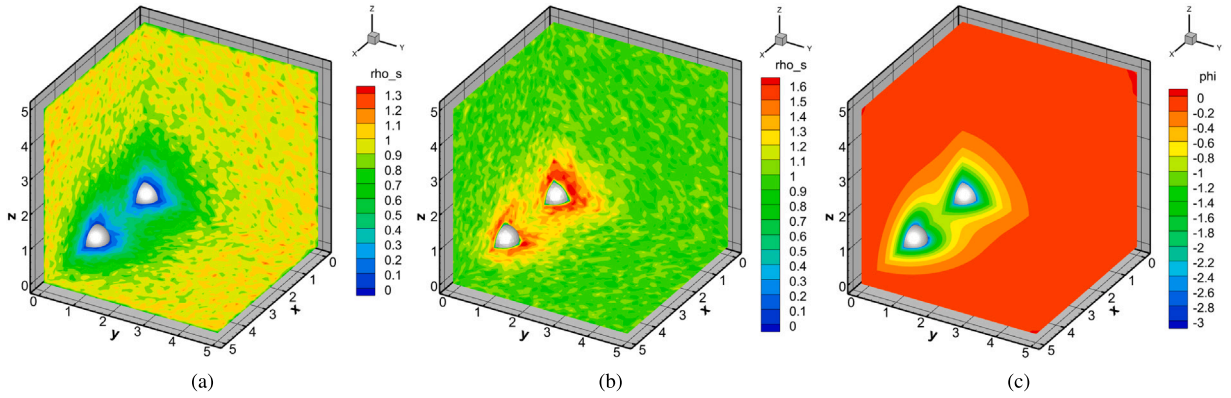

Fig. 6. Charging of two partial spherical dust grains with a normalized radius of 0.401 in a stationary experimental plasma including the (a) normalized electron density; (b) normalized ion density; and (c) normalized potential.

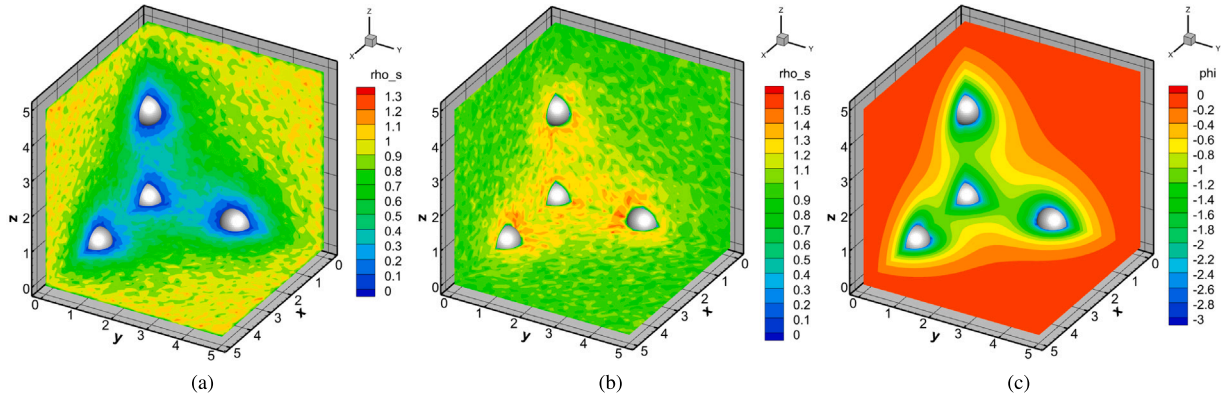

Fig. 7. Charging of four partial spherical dust grains with a normalized radius of 0.401 in a stationary experimental plasma including the (a) normalized electron density; (b) normalized ion density; and (c) normalized potential.

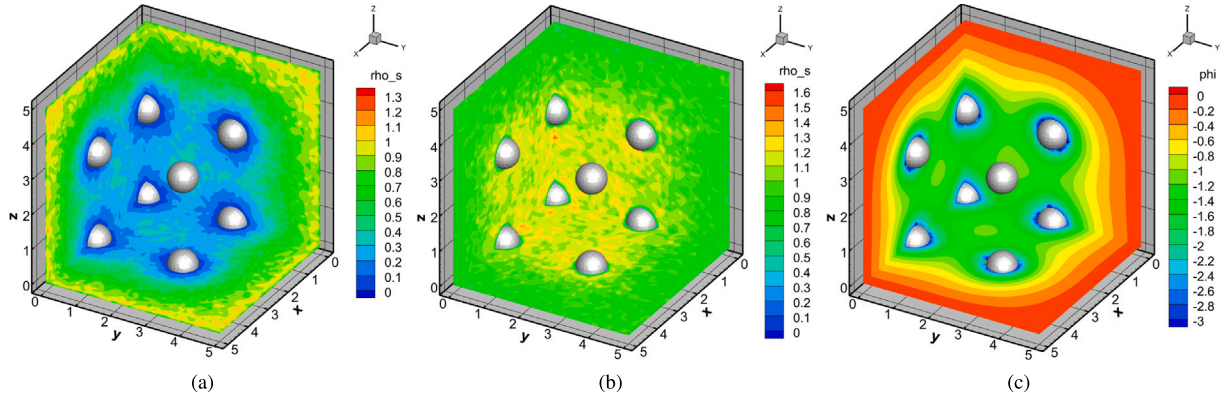

Fig. 8. Charging of eight partial spherical dust grains with a normalized radius of 0.401 and $1.7\lambda_D$ apart edge-to-edge in a stationary experimental plasma including the (a) normalized electron density; (b) normalized ion density; and (c) normalized potential.

Fig. 9a–c show the net surface charge ratio, Q_d/e, over time for multiple partial spherical dust grain configurations along with a single isolated grain of the same plasma conditions in a stationary experimental plasma. Where Fig. 9a has two partial dust grains, Fig. 9b has four partial dust grains, and Fig. 9c has eight partial dust grains. The legend in the plots list the isolated grain from Fig. 4 as well as dust grains 1 through 8 (which are the labeled dust grains from Fig. 3.) All the dust grains in this section have a normalized radius of $R_s = 0.401$. Again, due to symmetry of the domain the two partial dust grain case is actually three full dust grains in a straight line, the four partial dust grain case is a cluster of seven full dust grains, and the eight partial dust grain case is a cluster of twenty-seven full dust grains. For the eight partial grain configuration, there are four different types of grains: center of the cube (grain 1), cube corner (grain 8), face-centered (grains 2, 3, and 4), and edge-centered (grains 5, 6, and 7). These four types have been visually grouped with the color/line selection on the plots. The center

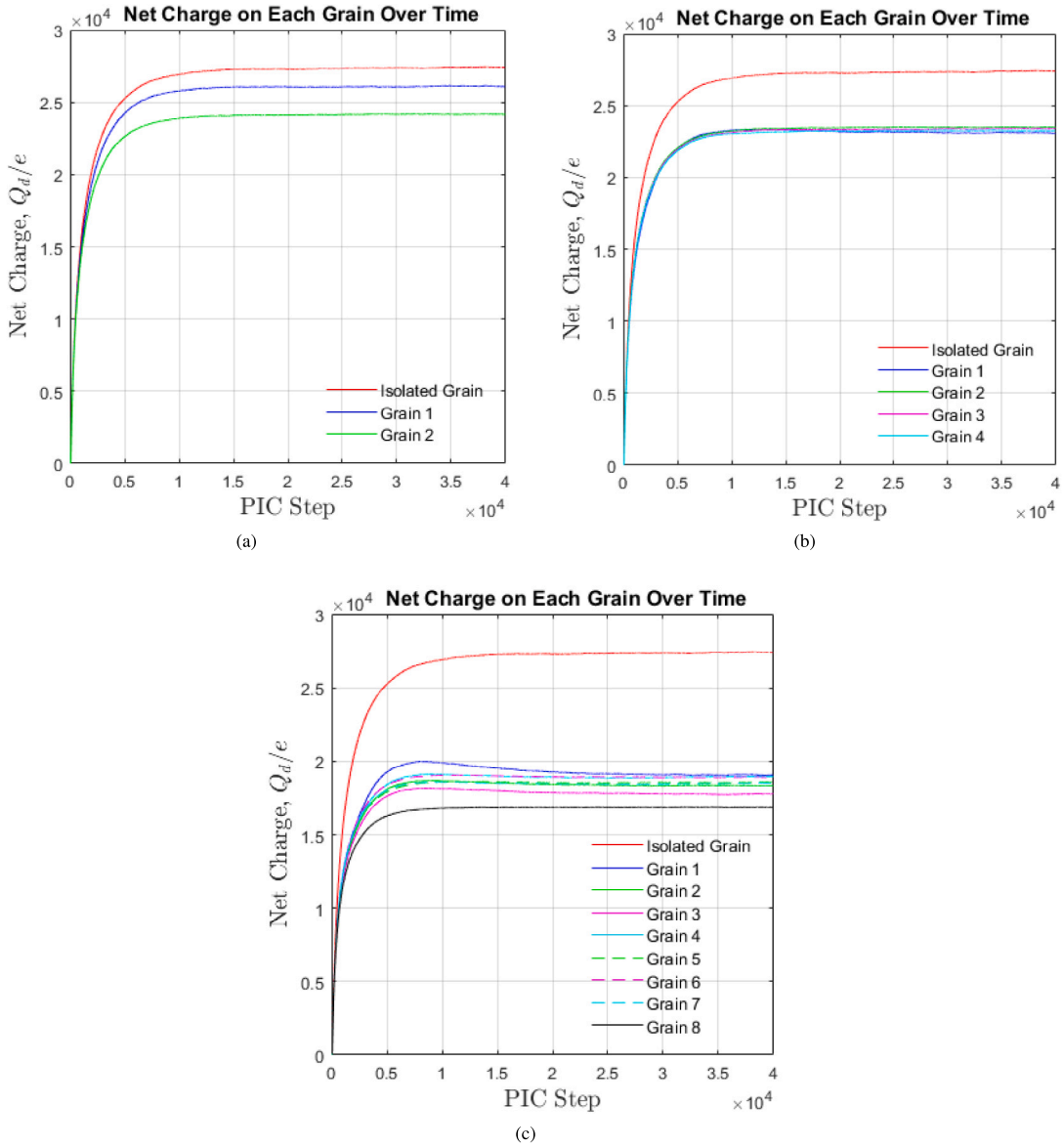

Fig. 9. Net surface charge for multiple partial spherical dust grain configurations along with a single isolated grain of the same plasma conditions in a stationary experimental plasma including (a) a collection of two spherical dust grains with a normalized radius of 0.401; (b) a collection of four spherical dust grains with a normalized radius of 0.401; and (c) a collection of eight spherical dust grains with a normalized radius of 0.401. (For interpretation of the references to colour in this figure legend, the reader is referred to the web version of this article.)

of the cube grain is marked as blue, the cube corner grain is marked as black, the face-centered grains are marked with solid green, magenta, and cyan lines, and the edge-centered grains are marked with dashed green, magenta, and cyan lines. This selection is also the same for the following subsection with varying distances.

The charge stops fluctuating around 15,000 PIC steps for the two and four partial dust grain cases, and all eight dust grains stop fluctuating around 25,000 for the eight partial dust grain case, which shows quasi steady-state being reached.

From Fig. 9, the three different configurations of partial dust grains (two, four, and eight) result in differing net surface charge ratios of the same magnitude. For reference, the single isolated grain of the same plasma conditions charges to a net surface charge ratio, Q_d/e, of approximately 2.74×10^4.

- The two partial dust grain case (Fig. 9a) shows a net surface charge ratio, Q_d/e, of 2.42×10^4 for the grain along the x-axis (grain 2) and 2.61×10^4 for grain at the origin (grain 1). Grain 1 charges more in this setup where three full dust grains are in a straight line. This is because both grains collect the same number of electrons, but grain 2 collects 1.5% more ions—resulting in a 7.6% increase of grain 1's net surface charge ratio. The center grain (grain 1) collects fewer ions because of their heavier nature, causing them to move in a relatively straight line resulting in more ions directly blocked by the outer grains (grain 2). On the other hand, the lighter and more mobile electrons can maneuver around the outer grains, leading to an equal deposition of negative charge on the grains. Both grain's net surface charge ratio is less than the single isolated grain of the same plasma conditions. Grain 1's net surface charge ratio is 1.32×10^3 less and grain 2's net surface charge ratio is 3.24×10^3 less than the single isolated grain.
- The four partial dust grain case (Fig. 9b) shows a net surface charge ratio, Q_d/e, of approximately 2.3×10^4 for all four dust grains. This group charged fairly identical, with a net surface charge ratio 4.4×10^3 lower than the single isolated grain of the

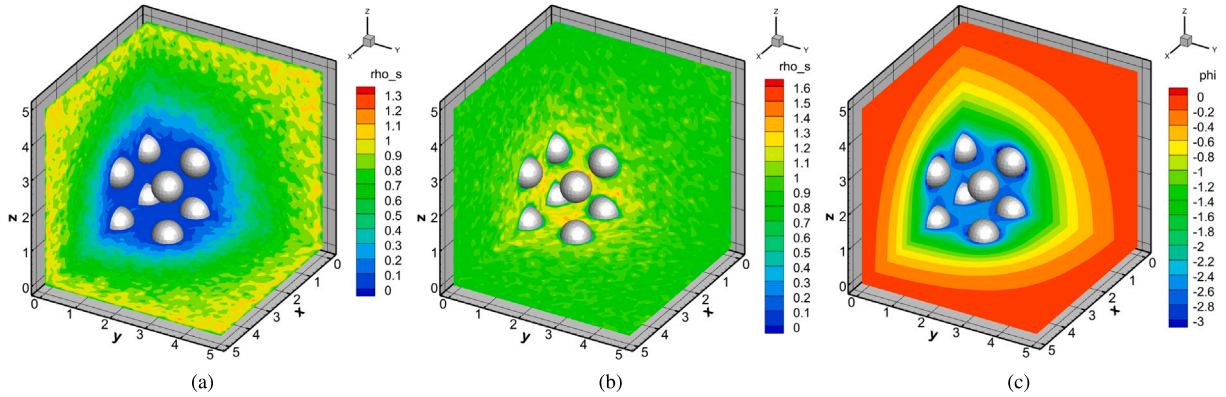

Fig. 10. Charging of eight partial spherical dust grains with a normalized radius of 0.401 and $0.7\lambda_D$ apart edge-to-edge in a stationary experimental plasma including the (a) normalized electron density; (b) normalized ion density; and (c) normalized potential.

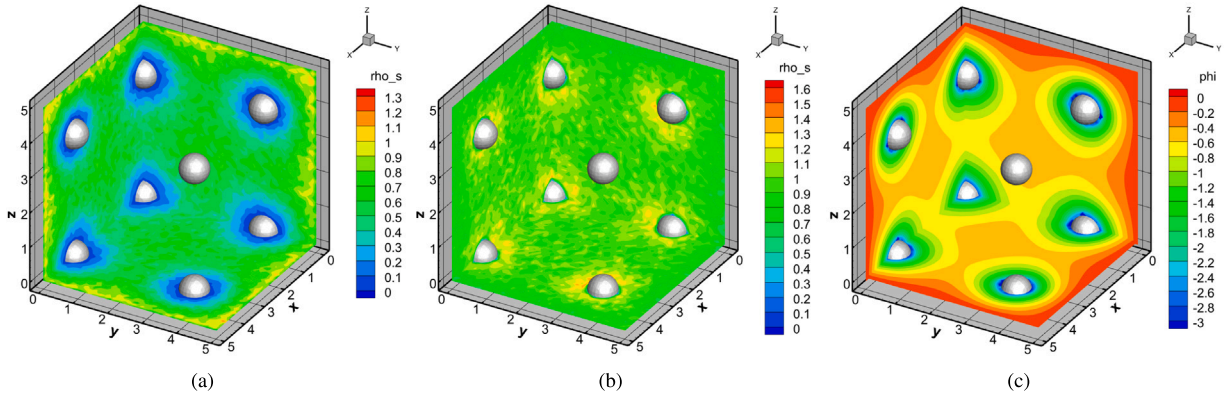

Fig. 11. Charging of eight partial spherical dust grains with a normalized radius of 0.401 and $2.7\lambda_D$ apart edge-to-edge in a stationary experimental plasma including the (a) normalized electron density; (b) normalized ion density; and (c) normalized potential.

same plasma conditions. Similar to the two partial grain case, fewer ions are able to impact the center grain (grain 1). However, due to more grains in the domain, the overall collected particles deceases, making the percentage difference of ions collected less noticeable. This results in a more similar net surface charge ratio for all four grains.

- The eight partial dust grain case (Fig. 9c) shows a net surface charge ratio, Q_d/e, in the range of 1.70×10^4 to 1.90×10^4 for the dust grains. This group charged similarly, although, with a bit more variability than the four partial dust grain case. Most likely due to the increased complexity of particle deposition from increasing the number of grains in the domain. Regardless, the trend continues with fewer ions impacting the center grain (grain 1) resulting in it having the highest net surface charge ratio. The average net surface charge ratio for the eight partial dust grains was 1.84×10^4, which is 9.02×10^3 lower than the single isolated grain of the same plasma conditions.

These results highlight that the net surface charge ratio on the dust grains is influenced by the number of surrounding dust grains. As the number of grains within in the domain increases, the average charge of the cluster strayed further away from the single isolated grain under the same plasma conditions. Again, these are expected results which have now been verified to further validate the code suite (Schleede et al., 2018; Matthews et al., 2016). This can be attributed to a fewer number of electrons and ions being able to deposit their charge on one specific dust grain as more dust grains block those impacts. For example, grain 2 in the two partial dust grain case collected 18,796,000 simulation electrons and 15,777,000 simulation ions, while grain 2 in the four partial dust grain case collected 18,185,000 simulation electrons and 15,250,000 simulation ions, and grain 2 in the eight partial dust grain case collected 15,571,000 simulation electrons and 13,279,000 simulation ions.

4. Discussion of novel results

In this section, novel results from the charging of dust grains in a stationary experimental plasma environment introduced in Section 3.2 are discussed. Specifically, how varying the electron Debye length edge-to-edge spacing among grains within a dust cluster changes the charging dynamics of the cluster, and introducing the first fully-kinetic simulations that vary the permittivity of the grain material while resolving an arbitrary irregular dust grain surface.

4.1. Varying distances for eight partial dust grain cases in a stationary experimental plasma environment

Figs. 10–11 illustrate the normalized density contours of the ions and electrons as well as the normalized potential surrounding the dust grains with varied distances apart for the eight partial dust grain case in a stationary experimental plasma. All the dust grains in this subsection have a radius of $R_s = 0.401$ and are all dielectric with a permittivity of 4. In Fig. 8, the original eight partial spherical dust grain case, the dust grains are spaced $1.7\lambda_D$ edge-to-edge from neighboring grains. In Fig. 10, the eight partial spherical dust grains are spaced $0.7\lambda_D$ edge-to-edge from neighboring grains. In Fig. 11, the eight partial spherical dust grains are spaced $2.7\lambda_D$ edge-to-edge from neighboring grains. These three configurations will show how the net surface charge ratio of the dust grains is influenced by their proximity to neighboring grains.

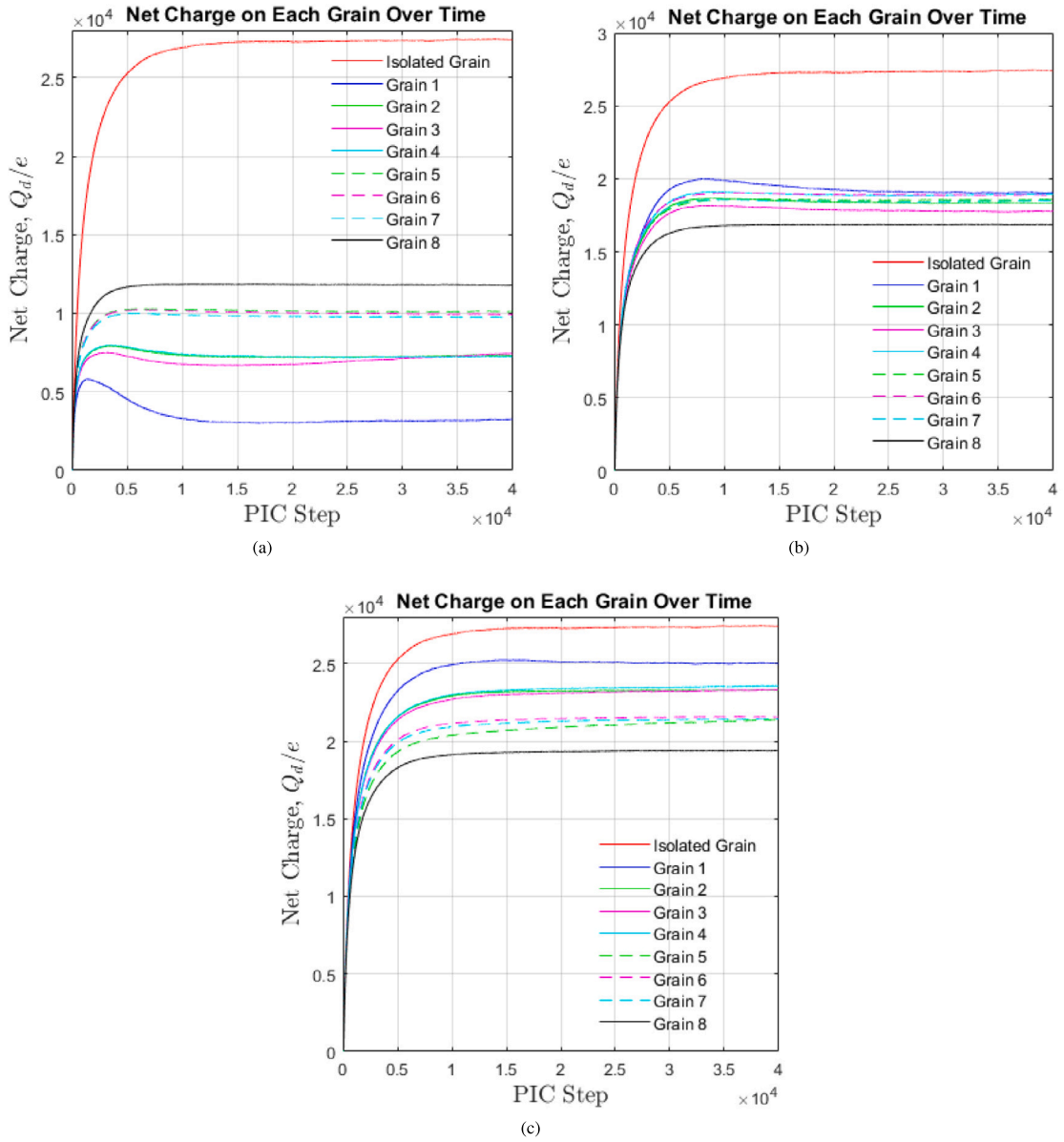

Fig. 12. Net surface charge ratio with varied distances apart for the eight partial dust grain case along with a single isolated grain of the same plasma conditions in a stationary experimental plasma including (a) a collection of eight partial spherical dust grains $0.7\lambda_D$ apart edge-to-edge, (b) a collection of eight partial spherical dust grains $1.7\lambda_D$ apart edge-to-edge, and (c) a collection of eight partial spherical dust grains $2.7\lambda_D$ apart edge-to-edge.

Fig. 12 shows the net surface charge ratio, Q_d/e, over time with varied distances apart for the three eight partial dust grain cases in a stationary experimental plasma. In Fig. 12a, the eight spherical dust grain's edges are $0.7\lambda_D$ apart. In Fig. 12b, the eight spherical dust grain's edges are $1.7\lambda_D$ apart. Finally, in Fig. 12c, the eight spherical dust grain's edges are $2.7\lambda_D$ apart. For the $0.7\lambda_D$ apart edge-to-edge case, the charge stops fluctuating around 15,000 PIC steps. For the $1.7\lambda_D$ apart edge-to-edge case, the charge stops fluctuating around 25,000 PIC steps. For the $2.7\lambda_D$ apart edge-to-edge case, the charge stops fluctuating around 10,000 PIC steps. Again, these results show quasi steady-state being reached.

From Fig. 12, all three varied distance cases resulted in significantly different net surface charge ratios on the grains within the cluster:

- The eight partial dust grain case $0.7\lambda_D$ edge-to-edge (Fig. 12a), shows a different net surface charge ratio, Q_d/e, for the four different types of grains. The center of the cube grain (grain 1) has the lowest net surface charge ratio of approximately 3.3×10^3. The face-centered grains (grains 2, 3, and 4) have the second lowest net surface charge ratio of approximately 7.3×10^3. The edge-centered grains (grains 5, 6, and 7) have the second highest net surface charge ratio of approximately 1.0×10^4. Finally, the cube corner grain (grain 8) has the highest net surface charge ratio of approximately 1.2×10^4.
- The eight partial dust grain case $1.7\lambda_D$ edge-to-edge (Fig. 12b), shows a similar net surface charge ratio, Q_d/e, for all of the partial grains. The grains all had a net surface charge ratio within the range of 1.7×10^4 to 1.9×10^4.
- The eight partial dust grain case $2.7\lambda_D$ edge-to-edge (Fig. 12b), shows a different net surface charge ratio, Q_d/e, for the four different types of grains. The center of the cube grain (grain 1) now has the highest net surface charge ratio of approximately 2.5×10^4. The face-centered grains (grains 2, 3, and 4) now have the second highest net surface charge ratio of approximately 2.3×10^4. The edge-centered grains (grains 5, 6, and 7) now have the second lowest net surface charge ratio of approximately 2.1×10^4.

Finally, the cube corner grain (grain 8) now has the lowest net surface charge ratio of approximately 1.9×10^4.

The relationship of different distances between grain clusters can be described by the following: For the eight partial spherical dust grain case separated by $2.7\lambda_D$ edge-to-edge, there is a potential gradient between the neighboring grains, shown in Fig. 11c. The normalized potential transitions from −3 immediately surrounding the grain to −0.3 halfway between adjacent grains then transitions back to −3 while approaching the next grain. The observed potential gradient occurs when the grains have ample separation to inflict minimal influence on the particle blockage or electric fields of adjacent grains. This separation causes the grains to charge much closer to that of the isolated grain case due to the grain having sufficient distance to fully shield itself, especially, noticeable in grain 1, shown in Fig. 12c. Grain 8 accumulates the lowest negative charge from being too close to the domain boundary, which has a fixed potential of 0. Ideally, if the domain was large enough, all eight grains would charge similarly. Since grain 1 is very close to being shielded at a $2.7\lambda_D$ edge-to-edge distance, a cutoff of $3.0\lambda_D$ edge-to-edge is enough for the potential from the shielded grain to drop to nearly zero. Thus it is recommended, $3.0\lambda_D$ should be the cutoff distance in numerical simulations for the interaction of charged dust grains in a group to be treated as isolated grains.

For the eight partial spherical dust grain case separated by $1.7\lambda_D$ edge-to-edge, the potential gradient between the grains disappears, shown in Fig. 8c. The normalized potential immediately surrounding the grain is again −3. However, between the grains is now uniformly −1.4, eliminating any sign of a potential gradient like that observed in the $2.7\lambda_D$ edge-to-edge case. The lack of a potential gradient indicates the grains are close enough to influence the particle blockage or electric fields of adjacent grains. This is evident in Fig. 12b, where all the grains charge much lower than the isolated grain case. The net surface charge ratios range between 1.7×10^4 and 1.9×10^4 with an average net surface charge ratio of 1.8×10^4, which is 9.0×10^3 lower than the isolated grain case's net surface charge ratio of 2.7×10^4. Also shown in Fig. 8c, these grains are far enough from the domain boundary to not be affected by its fixed 0 potential. Even though variable charging between the four different type of grain positions occur (center of the cube, cube corner, face-centered, and edge-centered), the percentage difference in grain charging is only 10%. Therefore, a separation distance around $1.7\lambda_D$ edge-to-edge should be considered acceptable for a dust cluster to charge uniformly.

As the eight partial spherical dust grains become even closer, only separated by $0.7\lambda_D$ edge-to-edge, the individual grains start to resemble a conglomeration of grains. The shrinking space between the grains has a normalized potential of −2.4 but still −3 immediately surrounding the grains, shown in Fig. 10c. This localized negative potential heavily attracts ions while concurrently repelling electrons. The increased ion density is shown by the normalized ion density of 1.4 in Fig. 10b compared to the normalized ion density of 0.7 for the dust grain case separated $2.7\lambda_D$ edge-to-edge in Fig. 11b. The decreased electron density is shown by the 0 normalized electron density in Fig. 10a compared to the normalized electron density of 0.7 for the dust grain case separated $2.7\lambda_D$ edge-to-edge in Fig. 11a. Due to the small space having a significant normalized negative potential of −2.4, only a small distribution of electrons posses enough energy to overcome the repulsive force to deposit their charge on the grain. This combination of particle attraction/repulsion reduces the negative charge on the grains, especially noticeable in the central grain (grain 1), shown in Fig. 12a. This can be quantified by comparing the number of particles collected by grain 1 in the $0.7\lambda_D$ edge-to-edge and $2.7\lambda_D$ edge-to-edge cases. For the grain 1 spaced $0.7\lambda_D$ edge-to-edge case, 11,898,000 simulations electrons deposit their charge, while for the $2.7\lambda_D$ edge-to-edge case, 16,362,000 simulations electrons deposit their charge. This highlights fewer electrons are able to deposit their charge on the central grain for the $0.7\lambda_D$ edge-to-edge case due to it being blocked by the surrounding grains. This makes it the most difficult grain for electrons to collide with and only allowing the most energized electrons to overcome the repulsion of the cluster.

Also, the four different types of grain positions clearly charge differently for this configuration based on their degree of immersion within the conglomeration. Since grain 8 is the outer most grain of the conglomeration, it has the highest probability for the energized electrons to collide with it. As a result, grain 8 has the most negative potential of the conglomeration with a net surface charge ratio of 1.2×10^4. The edge centered cubes (grains 5, 6, and 7), positioned as the second most outer group, have a net surface charge ratio approximately 1.7×10^3 less negative than grain 8. Following them, the face-centered cubes (grains 2, 3, and 4) have a net surface charge ratio approximately 4.5×10^3 less negative than grain 8. Lastly, the innermost grain, grain 1, charges the least negative, to a net surface charge ratio approximately 8.5×10^3 less negative than grain 8. If this conglomeration of grains continued to move closer, grain 1 would be completely engulfed resulting in its continual approach to a charge of 0 (basically acting as the immersed center of an aggregate grain.) Hence, a separation distance of approximately $0.7\lambda_D$ edge-to-edge or less should be considered acceptable for a dust cluster to be considered a conglomeration of particles. In reality, this is why aggregate grains should be considered instead of merely a conglomeration of spherical grains. Ultimately, the charging behavior of a dust cluster can be estimated by calculating its electron Debye length edge-to-edge separation to offer valuable insights into a dust cluster's general charge dynamics.

4.2. Varying shaped irregular dust grains in a stationary experimental plasma environment

This subsection presents the first fully-kinetic simulations to include and vary the dielectric permittivity of the grain material while resolving an arbitrary dust grain surface used to create an irregular dust grain immersed in a stationary experimental plasma environment. Unlike prior studies that focused solely on either fully conducting spheres or perfectly dielectric spheres, this work explores a more comprehensive range of permittivities which include permittivities of 4, 40, 400, and 4000. Two different irregular grain shapes with varying permittivities were simulated in this subsection. These irregular grains represent physical aggregate grains. To save space, only the irregular grains with a permittivity of 4 are shown in Figs. 13–14. These figures illustrate the normalized density contours of the ions and electrons as well as the normalized potential surrounding the irregular dust grains in a stationary experimental plasma.

The first irregular grain, shown in Fig. 13, consists of two partial spheres where an overlapping dust grain with half the normalized radius ($R_s = 0.201$) of the dust grain at the origin ($R_s = 0.401$) is extended in the x-direction. Due to symmetry, the two partial spheres are actually a linear triple-sphere cluster, where the two smaller attached spheres are the monomers of the aggregate. The second irregular grain, shown in Fig. 14, consists of two identical overlapping partial dust grains with half the normalized radius ($R_s = 0.201$) of the partial dust grain at the origin ($R_s = 0.401$) and are extended in the x- and y-directions. Again, due to symmetry, the three partial spheres represents a flat five-grain cluster (four grains surrounding a central grain), where the four smaller attached spheres are the monomers of the aggregate. The full 3-D models of the two irregular dust grains are shown in Fig. 15.

Fig. 16 shows the net surface charge ratio, Q_d/e, over time of two irregular dust grains along with a single isolated grain (normalized radius of $R_s = 0.401$) of the same plasma conditions in a stationary experimental plasma. For the irregular grain cases, the charge stops fluctuating around 20,000 PIC steps—resulting in quasi steady-state being reached. The two irregular dust grain configurations are shown in Fig. 16 with varying permittivity of 4, 40, 400, and 4000 along with an equivalent sphere with a permittivity of 4 to compare the results:

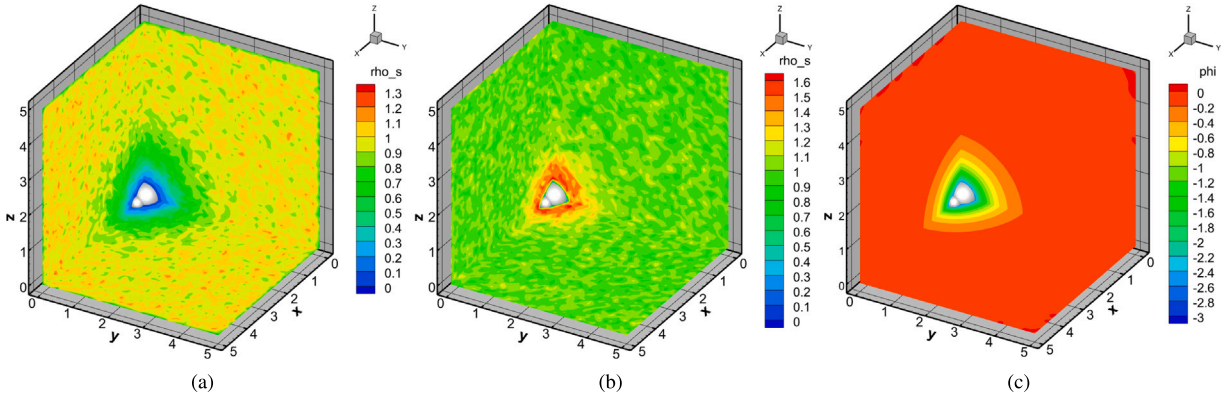

Fig. 13. Charging of a linear triple-sphere cluster in a stationary experimental plasma including the (a) normalized electron density; (b) normalized ion density; and (c) normalized potential.

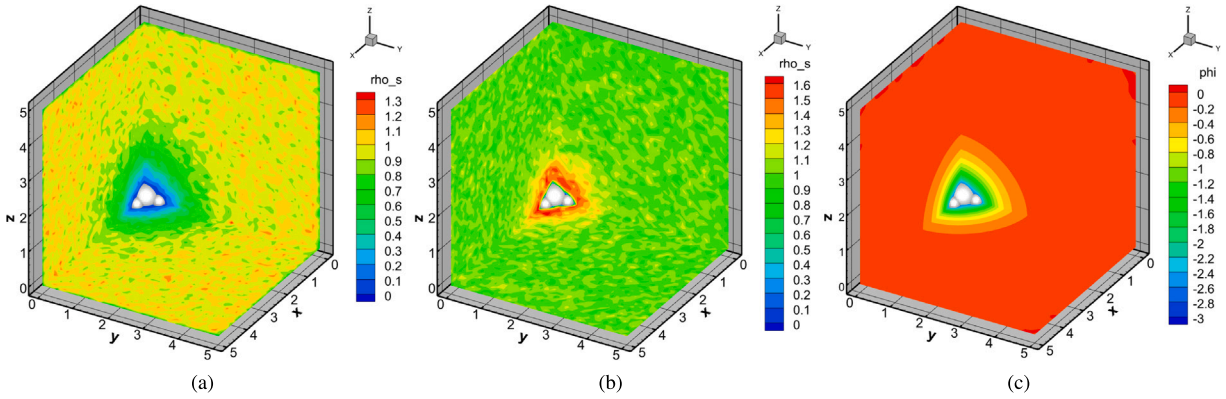

Fig. 14. Charging of a flat five-grain cluster in a stationary experimental plasma including the (a) normalized electron density; (b) normalized ion density; and (c) normalized potential.

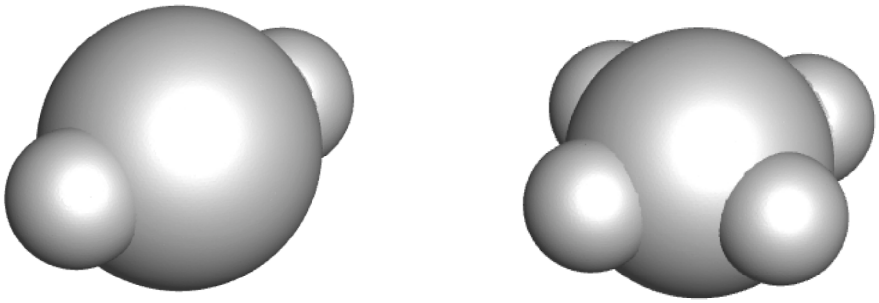

Fig. 15. 3-D models of the irregular dust grains including (a) a linear triple-sphere cluster and (b) a flat five-grain cluster.

- The equivalent sphere with a permittivity of 4 shows a net surface charge ratio, Q_d/e, of 2.77×10^4 which is used for comparison to the varying permittivity irregular grains.
- The first irregular dust grain is a linear triple-sphere cluster (Fig. 16a), which shows a net surface charge ratio, Q_d/e, of 3.02×10^4 for a permittivity of 4, a net surface charge ratio of 3.00×10^4 for a permittivity of 40, a net surface charge ratio of 3.02×10^4 for a permittivity of 400, and a net surface charge ratio of 3.1×10^4 for a permittivity of 4000 for the aggregates.
- The second irregular dust grain is a flat five-grain cluster (four grains surrounding a central grain) (Fig. 16b), which shows a net surface charge ratio, Q_d/e, of 3.24×10^4 for a permittivity of 4, a net surface charge ratio of 3.22×10^4 for a permittivity of 40, a net surface charge ratio of 3.26×10^4 for a permittivity of 400, and a net surface charge ratio of 3.38×10^4 for a permittivity of 4000 for the aggregates.

It is interesting that aggregates with lower permittivities (4, 40, and 400) all charge to a similar net surface charge ratio. The permittivity that stands out for both aggregates is the 4000 case. For the linear triple-sphere cluster, the percentage difference between the permittivity of 4000 and the group of 4, 40, and 400's net surface charge ratio is 3.3%, whereas for that of the flat five-grain cluster is 4.8%. Also, the normalized surface area of the linear triple-sphere cluster

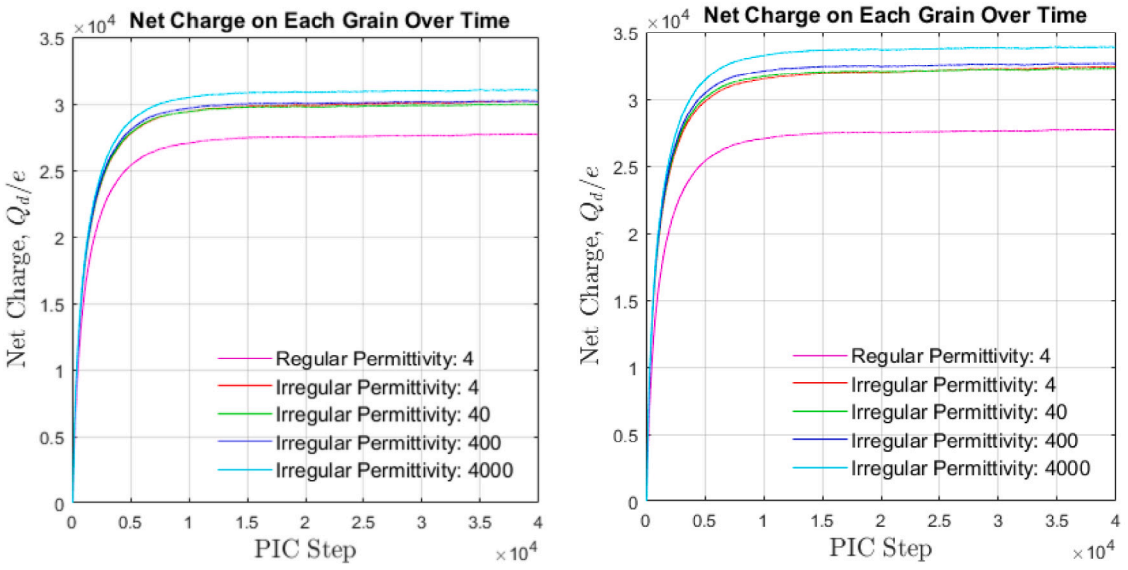

Fig. 16. Charging of irregular dust grains with varying permittivity along with a single isolated grain of the same plasma conditions in a stationary experimental plasma including (a) a linear triple-sphere cluster and (b) a flat five-grain cluster.

is 2.39 while that of the flat five-grain cluster is 2.76. Thus, the flat five-grain cluster has 14.3% more surface area than the linear triple-sphere cluster. This indicates that the importance of the permittivity, especially for conductors (where a perfect conductor has a permittivity of infinity), increases as the surface area of the aggregate increases. These results emphasize the crucial role of the grain's permittivity in determining its surface charge, especially when modeling conductors.

In contrast to the uniform charging observed in dielectric spheres (as discussed in Section 3.1), irregular aggregates lacking spherical symmetry do not exhibit uniform charging, shown in Fig. 17. On the surface of the aggregates, the normalized surface potential varies from −2.2 to −3 at different locations. The increasing permittivity leads to a more uniform surface potential (shown in Fig. 17c), highlighting the aggregates begin to mirror a conductor's property to spread out its charge. On the other hand, the more dielectric aggregates have patches of higher surface potential, creating equipotentials on the grain's surface (shown in Fig. 17a). This non-uniform behavior is a result of the absence of spherical symmetry in the irregular grains. Although aggregates with lower permittivities (4, 40, and 400) have similar net surface charge ratios, does not necessarily mean their surface charge is distributed proportionally. This is vital to consider when the charge distribution across the aggregate's surface can influence the charging of nearby grains differently. Therefore, these findings emphasize the grain's permittivity not only influences the overall net surface charge ratio but also its surface potential distribution. The non-uniform charging observed in irregular aggregates is attributed to the complex interplay between permittivity and shape irregularity, further highlighting the necessity to accurately consider irregular grain permittivity in simulations.

Finally, while the charging behavior of irregular grains can be estimated using the spherical grain case as a reference, these findings stress that this approach may serve as an underestimation. Adding a few monomers to the single isolated dielectric sphere increased its net surface charge ratio by 8.3% for the linear triple-sphere cluster and 15.6% for the flat five-grain cluster compared to the single isolated dielectric sphere. Thus, achieving accurate results demands explicit consideration of the grain's geometry and permittivity, especially in scenarios where non-uniform charging dynamics will be prominent.

5. Conclusion

This paper presents a comprehensive, fully-kinetic numerical investigation into the charging of dust grains within the OML sheath regime and a stationary experimental plasma. Utilizing the recently developed and highly parallel PIFE-PIC-D code, we explore the charge collection over time for each dust grain, considering variations in size, irregularity, the number of grains in the domain, spacing between dust grains, and permittivity.

A notable feature of this code is its capability to incorporate the dielectric permittivity of the grain material, allowing computation of the potential distribution over the grain's surface. This novel aspect extends our understanding of charging phenomena for both spherical and irregular dust grains. In contrast to prior studies that focused on fully conducting or perfectly dielectric spheres, this work explores a broader range of permittivities for irregular dust grain aggregates. The charging behavior of a dust cluster can be estimated by calculating its electron Debye length edge-to-edge separation to offer valuable insights into a dust cluster's general charge dynamics. Furthermore, this paper now introduces the first fully-kinetic simulations that vary the permittivity of the grain material while resolving an arbitrary dust grain surface used to created an irregular grain immersed in a stationary experimental plasma environment. These findings emphasize the grain's permittivity not only influences the overall net surface charge ratio but also its surface potential distribution. While estimating the charging behavior of irregular grains using the spherical grain case as a reference is common, our findings emphasize that this approach may underestimate results. Thus, achieving accurate results demands explicit consideration of the grain's geometry and permittivity, especially in scenarios where non-uniform charging dynamics will be prominent.

The reported results, along with ongoing research, contribute to addressing a fundamental question in dusty plasma: determining the net amount of charge and distribution on each individual dust grain. In our simulation setup, the net charge ratio (Q_d/e) is on the order of approximately 10^4. Our current focus is now on further exploring how spherical and irregular-shaped grains charge in a drifting plasma, understanding the effects of net charge near a surface, and conducting comparisons between simulation and experimental results. This ongoing work aims to enhance the understanding of complex dusty plasma dynamics.

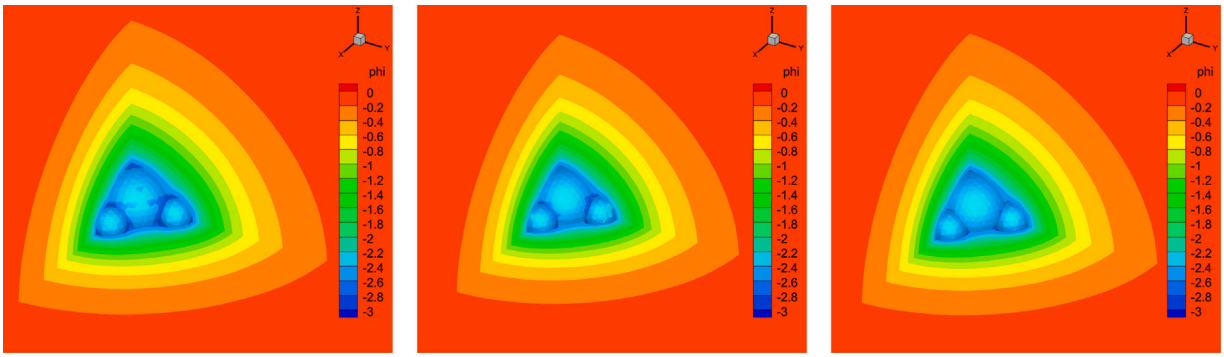

Fig. 17. Interpolated normalized surface potential of a flat five-grain cluster in a stationary experimental plasma highlighting the dielectric aggregate grain does not exhibit uniform surface charging including varying permittivities of (a) 4, (b) 40, and (c) 400.

CRediT authorship contribution statement

David Lund: Writing – review & editing, Writing – original draft, Visualization. **Nikolaos A. Gatsonis:** Project administration, Investigation, Funding acquisition. **Daoru Han:** Writing – review & editing, Writing – original draft, Supervision, Software, Resources, Project administration, Methodology, Investigation, Funding acquisition, Data curation, Conceptualization.

Declaration of competing interest

The authors declare that they have no known competing financial interests or personal relationships that could have appeared to influence the work reported in this paper.

Data availability

Data will be made available on request.

Acknowledgments

This work was partially supported by NASA through Physical Sciences Informatics (PSI) program (D.L., N.A.G., and D.H.), a NASA Space Technology Graduate Research Opportunity award (D.L.), and NASA-Missouri Space Grant Consortium graduate scholarships (D.L.). D.H. would also like to acknowledge the support from National Science Foundation through grants DMS-2111039 and CBET-2132655. The simulations presented here were performed with computing resources provided by the Center for High Performance Computing Research at Missouri University of Science and Technology through an National Science Foundation grant OAC-1919789.

References

Abbas, M.M., Tankosic, D., Craven, P.D., Spann, J.F., LeClair, A., West, E.A., 2007. Lunar dust charging by photoelectric emissions. Planet. Space Sci. 55 (7–8), 953–965.

Anuar, A.K., Honary, F., Hapgood, M., Roussel, J.-F., 2013. Three-dimensional simulation of dust charging and dusty plasma using spis. J. Geophys. Res. Space Phys. 118 (10), 6723–6735.

Asnaz, Ogu Han, Jung, Hendrik, Greiner, Franko, Piel, Alexander, 2018. Charging of an irregularly shaped particle in the sheath of an rf plasma. Phys. Plasmas 25 (7), 073702.

Bouchoule, André, 1999. Dusty Plasmas: Physics, Chemistry, and Technological Impact in Plasma Processing. Wiley.

Chahl, Harjinda Singh, Gopalakrishnan, Ranganathan, 2019. High potential, near free molecular regime coulombic collisions in aerosols and dusty plasmas. Aerosol Sci. Technol. 53 (8), 933–957.

Conger, J., Hastings, D., 1992. Control of particle-spacecraft interactions in a leo near-spacecraftenvironment. In: 31st Aerospace Sciences Meeting. AIAA 93-0566, Reno, NV, U.S.A.

Cui, Chunshi, Goree, John, 1994. Fluctuations of the charge on a dust grain in a plasma. IEEE Trans. Plasma Sci. 22, 151–158.

Delzanno, Gia Luca, Tang, Xian-Zhu, 2015. Comparison of dust charging between orbital-motion-limited theory and particle-in-cell simulations. Phys. Plasmas 22, 113703.

Ding, Ning, Wang, Joseph, Polansky, John, 2013. Measurement of dust charging on a lunar regolith simulant surface. IEEE Trans. Plasma Sci. 41 (12), 3498–3504.

Erlandson, Robert E., Gatsonis, N.A., 1994. Particle-in-cell/Monte Carlo simulation of dusty plasmas near spacecraft surfaces. In: Peter, A., Glassford, M. (Eds.), Optical System Contamination: Effects, Measurements, and Control IV. Vol. 2261, International Society for Optics and Photonics, SPIE, pp. 126–134.

Flanagan, T.M., Goree, J., 2006. Dust release from surfaces exposed to plasma. Phys. Plasmas 13 (12), 123504.

Gatsonis, N.A., Erlandson, R.E., Meng, C.I., 1994. Simulation of dusty plasmas near surfaces in space. J. Geophys. Res. Space Phys. 99 (A5), 8479–8489.

Gopalakrishnan, Ranganathan, Hogan, Christopher J., 2012. Coulomb-influenced collisions in aerosols and dusty plasmas. Phys. Rev. E 85 (2).

Han, Daoru, He, Xiaoming, Lund, David, Zhang, Xu, 2021. PIFE-PIC: Parallel immersed finite element particle-in-cell for 3-D kinetic simulations of plasma-material interactions. SIAM J. Sci. Comput. 43 (3), C235–C257.

Han, Daoru, He, Xiaoming, Wang, Joseph J., 2018. PIFE-PIC: A 3-D parallel immersed finite element particle-in-cell framework for plasma simulations. In: AIAA SciTech Forum 2018. AIAA 2018-2196, Kissimmee, Florida.

Han, D., Wang, J., He, X.-M., 2016a. A non-homogeneous immersed-finite-element particle-in-cell method for modeling dielectric surface charging in plasmas. IEEE Trans. Plasma Sci. 44 (8), 1326–1332.

Han, Daoru, Wang, P., He, Xiaoming, Lin, Tao, Wang, Joseph, 2016b. A 3d immersed finite element method with non-homogeneous interface flux jump for applications in particle-in-cell simulations of plasma–lunar surface interactions. J. Comput. Phys. 321, 965–980.

He, Xiaoming, Lin, Tao, Lin, Yanping, 2008. Approximation capablity of a bilinear immersed finite element space. Numer. Methods Partial Differential Equations 24 (5), 1265–1300.

He, Xiaoming, Lin, Tao, Lin, Yanping, 2011. Immersed finite element methods for elliptic interface problems with non-homogeneous jump conditions. Int. J. Numer. Anal. Model. 8 (2), 284–301.

Hess, S.L.G., Sarrailh, P., Matéo-Vélez, J.-C., Jeanty-Ruard, B., Cipriani, F., Forest, J., Hilgers, A., Honary, F., Thiébault, B., Marple, S.R., Rodgers, D., 2015. New spis capabilities to simulate dust electrostatic charging, transport, and contamination of lunar probes. IEEE Trans. Plasma Sci. 43 (9), 2799–2807.

Kafafy, Raed I., Wang, Joseph, 2006. A hybrid grid immersed finite element particle-in-cell algorithm for modeling spacecraft-plasma interactions. IEEE Trans. Plasma Sci. 34 (5), 2114–2124.

Khrapak, S.A., Morfill, G.E., Fortov, V.E., D'yachkov, L.G., Khrapak, A.G., Petrov, O.F., 2007. Attraction of positively charged particles in highly collisional plasmas. Phys. Rev. Lett. 99.

Lund, David, He, Xiaoming, Zhang, X., Han, Daoru, 2022. Weak scaling of the parallel immersed-finite-element particle-in-cell (pife-pic) framework with lunar plasma charging simulations. Comput. Part. Mech. 9, 1279–1291.

Matsoukas, Themis, Russell, Marc, 1997. Fokker-Planck description of particle charging in ionized gases. Phys. Rev. E 55, 991–994.

Matthews, Lorin S., Coleman, Douglas A., Hyde, Truell W., 2016. Multipole expansions of aggregate charge: How far to go? IEEE Trans. Plasma Sci. 44 (4), 519–524.

Matthews, Lori Swint, Sanford, Dustin L., Kostadinova, Evdokiya G., Ashrafi, Khandake Sharmin, Guay, Evelyn, Hyde, Truell W., 2020. Dust charging in dynamic ion wakes. Phys. Plasmas 27 (2), 023703.

Matthews, Lorin S., Shotorban, Babak, Hyde, Truell W., 2013. Cosmic dust aggregation with stochastic charging. Astrophys. J. 776 (2), 103.

Matyash, K., Schneider, R., Ikkurthi, R., Lewerentz, L., Melzer, A., 2010. P3M simulations of dusty plasmas. Plasma Phys. Control. Fusion 52 (12), 124016.
Melzer, A., Trottenberg, T., Piel, A., 1994. Experimental determination of the charge on dust particles forming coulomb lattices. Phys. Lett. A 191 (3), 301–308.
Northrop, T.G., Birmingham, T.J., 1996. Equilibrium electric potential of spherical, cylindrical, and planar dust grains moving through a plasma. J. Geophys. Res. Space Phys. 101 (A5), 10793–10796.
Oudayer, P., Monnin, L., Matéo-Vélez, J.-C., Hess, S.L.G., Sarrailh, P., Murat, G., Roussel, J.-F., 2019. Multiscale modeling of dust charging in simulated lunar environment conditions. IEEE Trans. Plasma Sci. 47 (8), 3710–3716.
Picard, Romai Le, Girshick, Steven L, 2016. The effect of single-particle charge limits on charge distributions in dusty plasmas. J. Phys. D: Appl. Phys. 49 (9), 095201.
Robertson, S., Walch, B., Horányi, M., 1995. Charging of dust grains in plasma with energetic electrons. Phys. Rev. Lett. 75 (5), 838–841.
Schleede, J., Lewerentz, L., Bronold, F.X., Schneider, R., Fehske, H., 2018. Plasma flow around and charge distribution of a dust cluster in a rf discharge. Phys. Plasmas 25 (4), 043702.
Sharma, S.K., Kalita, R., Nakamura, Y., Bailung, H., 2012. Dust charge measurement in a strongly coupled dusty plasma produced by an rf discharge. Plasma Sources Sci. Technol. 21 (4), 045002.
Shotorban, B., 2014. Intrinsic fluctuations of dust grain charge in multi-component plasmas. Phys. Plasmas 21 (3), 033702.
Smith, Barry, Bjørstad, Petter, Gropp, William, 1996. Domain Decomposition: Parallel Multilevel Methods for Elliptic Partial Differential Equations. Cambridge University Press.
Smith, M.A., Goodrich, J., Rahman, H.U., Mohideen, U., 2001. Measurement of grain charge in dusty plasma coulomb crystals. IEEE Trans. Plasma Sci. 29 (2), 216–220.
Tang, Xian-Zhu, Delzanno, Gian Luca, 2014. Orbital-motion-limited theory of dust charging and plasma response. Phys. Plasmas 21, 123708.
Vaulina, O.S., Khrapak, S.A., Nefedov, A.P., Petrov, O.F., 1999. Charge-fluctuation-induced heating of dust particles in a plasma. Phys. Rev. E.
Vijayan, Akhi Marayikkottu, Sawant, Saurabh S., Levin, Deborah A., Huang, C., Schoenitz, Mirko, Dreizin, Edward, 2020. Comparison of numerical simulations of inert particle transport in an electrostatic discharge with experimental results. In: AIAA Scitech 2020 Forum. AIAA 2020-1798, Orlando, FL.
Wang, X., Schwan, J., Hsu, H.-W., Grün, E., Horányi, M., 2016. Dust charging and transport on airless planetary bodies. Geophys. Res. Lett. 43 (12), 6103–6110.
Zhao, Jianxun, Yan, Guirong, Han, Daoru, 2021. A review of approaches to simulate windborne debris dynamics in wind fields. J. Wind Eng. Ind. Aerodyn. 212, 104597.
Zimmerman, M.I., Farrell, W.M., Hartzell, C.M., Wang, X., Horanyi, M., Hurley, D.M., Hibbitts, K., 2016. Grain-scale supercharging and breakdown on airless regoliths. J. Geophys. Res.: Planets 121 (10), 2150–2165.